

## VCST Internal Memo

**Title:** Analysis of Ambient Level RC-1 Part 1 Thermal Band Radiometric Characterization

**Memo Number:** 2014\_020

**Revision:** 01

**Date:** September 15, 2014

**Author:** Jeff McIntire

**To:** Xiaoxiong Xiong and James Butler

**Cc:** Hassan Oudrari, Kwo-Fu (Vincent) Chiang, Jon Fulbright and Aisheng Wu

---

### References

- [1] TP1544640-2230 Rev B, 'Radiometric Response and Sensitivity, Ambient (RC-1),' Raytheon.
- [2] VIIRS PRD Rev C, 'Joint Polar-orbiting Satellite System (JPSS) Visible Infrared Imaging Radiometer Suite (VIIRS) Performance Requirements Document (PRD).'
- [3] VCST\_TECH\_REPORT\_13\_015, 'Preliminary Results from RC-1 Part 1: B side,' Jeff McIntire, September 9, 2013.
- [4] VCST\_TECH\_REPORT\_13\_019, 'Preliminary Results from ETP-249 (RC-1 Part 1: Aside),' Jeff McIntire, September 19, 2013.
- [5] VCST\_TECH\_REPORT\_13\_046, 'Preliminary Results from RC-1 Part 1: A side,' Jeff McIntire, December 24, 2013.
- [6] VCST\_TECH\_REPORT\_14\_015, 'Summary of Preliminary Results from RC-1 Part 1,' Jeff McIntire, February 27, 2014.
- [7] NICST\_MEMO\_08\_022, 'Data Analysis Results for VIIRS FU1 TEB RC01 Test,' Sanxiong Xiong, Chunhui Pan, and Nianzeng Che, June 16, 2008.
- [8] F1\_RSR\_PVR\_JT\_091412, 'Performance Verification Report – VIIRS Relative Spectral Response (PVP Section 4.6),' Justin Trice, Nicholas Lardas, and Mark Bliton, December 4, 2009.
- [9] VCST\_TECH\_MEMO\_2014\_018, 'Analysis of FP-10 Part 2 Thermal Band Response Versus Scan Angle Determination,' Jeff McIntire, August 15, 2014.
- [10] NICST\_MEMO\_11\_001, 'Analysis of Radiometric Calibration from VIIRS F1 RC-05 Part 1 Test (Nominal Plateau, Electronic Side B),' Jeff McIntire and Sanxiong Xiong, January 3, 2011.
- [11] NICST\_MEMO\_11\_004, 'Experimental Determination of VIIRS Detector Saturation Levels,' Jeff Cronkhite and Jeff McIntire, April 21, 2011.

### 1. Introduction

The VIIRS F2 test RC-1 Part 1 was designed to examine the sensor response to well calibrated, external sources [the Lab Ambient Blackbody (LABB) and the Three Mirror Collimator (TMC) blackbody (BB)] referenced to a warm On-Board Calibrator Blackbody (OBC BB) in an ambient environment. This test consisted of two sections: low and high temperature. The low temperature portion was conducted at a series of discrete temperature levels for the LABB and TMC BB designed to access the full dynamic range of the single gain bands and M13 high gain. The high temperature segment was designed to calibrate the low gain sector of M13 using the TMC BB.

This work will focus on the radiometric calibration and sensitivity as well as on compliance with a number of specifications from the RC-1 test on electronic sides A and B [1,2]. Preliminary investigations of this test were reported in [3-6].

Tables 1 – 3 list the relevant UAIDs, collects, and gain modes in addition to the LABB, TMC BB, and OBC BB temperatures. The TMC BB and LABB sources were located at scan angles of -29.4 and 28.4 degrees respectively; the OBC BB was at 100 degrees scan angle.

The VIIRS sensor was in operational mode and each collect contains 40 scans. The sensor was set to fixed high gain for the low temperature portion; all three gain modes were measured for the high temperature sequence (although only fixed low gain is used in this work). Data was collected at both nominal and 60 % of nominal integration times (only the nominal integration time data is presented here). The cold focal planes were controlled at ~79.5 K. Additional limited testing in diagnostic mode was conducted with the cold focal planes at ~82.5 K (low temperature only). The general outline of the methodology used in this work follows from [7] with some modifications.

## 2. Test Setup and Analysis

The data analyzed here is restricted to a subset of the Earth View (EV) samples in a given collect for which the LABB or TMC BB source yielded a stable response. The sample ranges used in this work are listed in Table 3. All the samples for the OBC BB were analyzed.

The DN for the EV sector was truncated to 12 bits while the calibration sectors reported DN in 14 bits. This leads to a bias in the dn. As a result, all calibration view data used in this work was first truncated to 12 bits.

First, the  $DN_{OBCBB}$  was averaged over all samples in a given scan. Then, the sample averaged  $DN_{OBCBB}$  was subtracted from each sample of the  $DN_{EV}$  in the corresponding scan to produce the dn. Next, the dn was averaged over samples and the standard deviation of all samples for a specific scan was calculated. Note that the Half Angle Mirror (HAM) sides alternate from scan to scan such that there are 20 scans for each HAM side. Additionally, the I band data is divided into two subsamples; the larger for OBC BB is always matched to the larger for the EV (using the same aggregation method employed by the  $DN_{EV}$  of interest) to ensure the proper background subtraction. Lastly, the dn and standard deviation are averaged over scans (each HAM side separately).

Some small non-uniformity was observed in the scan direction on the LABB. This non-uniformity generally decreased the SNR. However, this non-uniformity is expected to be much smaller in thermal vacuum testing, and that analysis will supersede the ambient performance reported here.

The temperatures ( $T_{xxx}$ ) of the following were extracted: LABB, OBC BB, TMC BB, HAM, Rotating Telescope Assembly (RTA), scan CAVity (CAV), and OBC BB SHield (SH). The OBC BB, HAM, CAV, and SH temperatures were acquired using the LRV telemetry extractor while the LABB and TMC BB temperatures were obtained from the Ground Support Equipment (GSE) files. The RTA temperature is derived using the CAV temperature minus 8 degrees K.

### 2.1 Radiometric Calibration – Single Gain and M13 High Gain

In this section, the calibration of the single gain bands and M13 high gain are considered. The discussion of the M13 low gain calibration using the TMC BB will be discussed in a later section.

For each of the extracted temperatures, the Planck radiance at a given wavelength is calculated from

$$L_{xxx}(C, \lambda, T_{xxx}(C)) = \frac{2hc^2}{\lambda^5} \frac{1}{e^{hc/\lambda kT_{xxx}} - 1} \quad (1)$$

where C refers to collect. The radiance for a particular band and detector is determined by weighting the Planck radiance by the Relative Spectral Response (RSR) over the In-Band (IB) region (between the 1% response points), or

$$\langle L_{xxx}(C, B, D) \rangle = \frac{\int_{IB} RSR(B, D, \lambda) L_{xxx}(C, \lambda, T_{xxx}) d\lambda}{\int_{IB} RSR(B, D, \lambda) d\lambda} \quad (2)$$

where B and D represent band and detector, respectively. VIIRS F1 RSR was used here, provided by the Raytheon [8] (VIIRS F2 RSR has not yet been measured). Because the external source temperatures are not recorded on a scan basis, their radiances are determined on a collect basis. In contrast, the internal source temperatures are recorded on a scan basis; in this work the collect average is used.

The effective OBC BB radiance is

$$\begin{aligned} \langle L_{OBCBB}(C, B, H, D) \rangle_{eff} &= \varepsilon_{OBCBB}(B) \langle L_{OBCBB}(C, B, H, D) \rangle \\ &- [1 - \varepsilon_{OBCBB}(B)] [F_{CAV} \langle L_{CAV}(C, B, H, D) \rangle \\ &+ F_{SH} \langle L_{SH}(C, B, H, D) \rangle + F_{RTA} \langle L_{RTA}(C, B, H, D) \rangle] \end{aligned} \quad (3)$$

where  $\varepsilon_{OBCBB}$  is the emissivity of the OBC BB and H represents the HAM side.  $F_{CAV}$ ,  $F_{SH}$ , and  $F_{RTA}$  are the shape factors related to the solid angles of the CAV, SH, and RTA as viewed by the OBC BB; these factors determine the reflectance off the OBC BB.

The at-detector path difference radiance between the LABB and the OBC BB is

$$\begin{aligned} \Delta L_{LABB}(C, B, H, D) &= r_{VS}(B, H, D, \phi_{LABB}) \langle L_{LABB}(C, B, D) \rangle \\ &- r_{VS}(B, H, D, \phi_{OBCBB}) \langle L_{OBCBB}(C, B, H, D) \rangle_{eff} \\ &- \frac{[r_{VS}(B, H, D, \phi_{OBCBB}) - r_{VS}(B, H, D, \phi_{LABB})]}{\rho_{RTA}(B)} \\ &\times [\langle L_{HAM}(C, B, D) \rangle - (1 - \rho_{RTA}(B)) \langle L_{RTA}(C, B, D) \rangle] \end{aligned} \quad (4)$$

The radiances are corrected for Response Versus Scan (RVS) angle and the reflectance factor of the RTA optics ( $\rho_{RTA}$ ). Note that  $\phi$  refers to the HAM angle of incidence for the LABB or OBC BB source [the RVS is normalized to 1.0 at the Space View (SV) HAM angle]. The RVS used in this work was derived from F2 testing [9].

The background subtracted radiance is modeled by a polynomial in the detector response. These polynomials take the form

$$\Delta L_{LABB}(C, B, H, D) = \sum_{i=0}^N c_i^{LABB}(B, H, D) d_{LABB}^i(C, B, H, D) \quad (5)$$

Least-squares fits were performed over the dynamic range at the linear, quadratic, and cubic levels (or order N) to determine the polynomial coefficients. Data for which the SNR was below 1.0 was excluded from the fitting. The inverse of the linear term ( $1/c_1$ ) is the radiometric gain (detector responsivity).

Lastly, the retrieved calibration LABB radiance is defined as

$$\begin{aligned}
\left\langle L_{LABB} (C, B, H, D) \right\rangle_{ret} &= \frac{\sum_{i=0}^N c_i^{LABB} (B, H, D) dn_{LABB}^i (C, B, H, D)}{r_{VS}^{LABB} (B, H, D, \phi_{LABB})} \\
&+ r_{VS} (B, H, D, \phi_{OBCBB}) \left\langle L_{OBCBB} (C, B, H, D) \right\rangle_{eff} \quad (6) \\
&+ \frac{[r_{VS} (B, H, D, \phi_{OBCBB}) - r_{VS} (B, H, D, \phi_{LABB})]}{\rho_{RTA} (B)} \\
&\times [\left\langle L_{HAM} (C, B, D) \right\rangle - (1 - \rho_{RTA} (B)) \left\langle L_{RTA} (C, B, D) \right\rangle]
\end{aligned}$$

## 2.2 Radiometric Calibration – M13 Low Gain

The low gain radiometric calibration for M13 was performed separately from the high gain and all the thermal single gain bands. The LABB source has a maximum temperature of ~360 K, which is at the very low end of the M13 low gain dynamic range. As a result, the TMC BB is used to access the high temperature region. The TMC BB radiance is modeled as

$$\begin{aligned}
\Delta L_{TMCBB} (C, B, H, D) &= r_{VS} (B, H, D, \phi_{TMCBB}) \varepsilon_{TMCBB} (B) \left\langle L_{TMCBB} (C, B, D) \right\rangle \\
&- r_{VS} (B, H, D, \phi_{OBCBB}) \left\langle L_{OBCBB} (C, B, H, D) \right\rangle_{eff} \quad (7) \\
&- \frac{[r_{VS} (B, H, D, \phi_{OBCBB}) - r_{VS} (B, H, D, \phi_{TMCBB})]}{\rho_{RTA} (B)} \\
&\times [\left\langle L_{HAM} (C, B, D) \right\rangle - (1 - \rho_{RTA} (B)) \left\langle L_{RTA} (C, B, D) \right\rangle]
\end{aligned}$$

The TMC emissivity was determined by cross-calibrating to the LABB in the low temperature region (below 345 K). The cross-calibration is accomplished by assuming that

$$\Delta L_{TMCBB} (C, B, H, D) = \sum_{i=0}^N a_i^{LABB} (B, H, D) dn_{TMCBB}^i (C, B, H, D), \quad (8)$$

and then solving Eq. (7) for the TMC BB emissivity using low temperature data. This emissivity is applied to the high temperature collects in fixed low gain, through Eq. (7). Then, the calculated high temperature radiance is related to the dn by the following:

$$\Delta L_{TMCBB} (C, B, H, D) = \sum_{i=0}^N c_i^{TMCBB} (B, H, D) dn_{TMCBB}^i (C, B, H, D). \quad (9)$$

The coefficients are determined through least-squares fitting. Lastly, the retrieved calibration TMC BB radiance is defined as

$$\begin{aligned}
\left\langle L_{TMCBB} (C, B, H, D, S) \right\rangle_{ret} &= \frac{\sum_{i=0}^N c_i^{TMCBB} (B, H, D) dn_{TMCBB}^i (C, B, H, D)}{r_{VS}^{TMC} (B, H, D, \phi_{TMCBB})} \\
&+ r_{VS} (B, H, D, \phi_{OBCBB}) \left\langle L_{OBCBB} (C, B, H, D) \right\rangle_{eff} \quad (10) \\
&+ \frac{[r_{VS} (B, H, D, \phi_{OBCBB}) - r_{VS} (B, H, D, \phi_{TMCBB})]}{\rho_{RTA} (B)} \\
&\times [\left\langle L_{HAM} (C, B, D) \right\rangle - (1 - \rho_{RTA} (B)) \left\langle L_{RTA} (C, B, D) \right\rangle]
\end{aligned}$$

## 2.3 Radiometric Sensitivity and Specifications

The radiometric sensitivity and specifications [2] associated with thermal band radiometric calibration were calculated as described in [10] (NEdT at  $T_{\text{TYP}}$ , RRNL, RRCU, ARD, and RRU). The methodology used for saturation determination was described in [11]. Note that the gain transition analysis is described elsewhere (in conjunction with RC-01 part 4) and that for VIIRS F2 sensor nonlinearity is no longer a requirement.

### 3. Analysis

#### 3.1 Radiometry

The thermal band radiance, fit using a quadratic polynomial in dn, are shown in Figure 1 for all high gain bands and all detectors (HAM A and electronics side A). The corresponding radiance residual for each high gain band is shown in Figure 2. The residual is generally small for the LWIR bands I5 and M14 – M16 (less than 0.5 %). The residuals for I4, M12, and M13 in particular increase at lower temperatures (up to 2% at  $T_{\text{MIN}}$ ); these bands are known to exhibit greater nonlinearity at low radiances. The results for electronics side B are shown in Figures 3 and 4. There was a discontinuity in the cold focal plane temperature between the third and fourth LABB levels of about 0.2 K; this is visible in the residuals (compare to Figure 2). The fitting and residuals from additional testing with the cold focal planes at ~82.5 K is shown in Figures 5 and 6 (on electronics side A). Residuals were comparable to earlier electronics side A testing. Although only HAM side A was shown, both HAM sides yield very similar results.

The median high gain calibration coefficients for a quadratic polynomial fit are given in Tables 5 – 7 for electronics sides A and B as well as for the elevated cold focal planes temperatures measured for side A. Note that the offset term ( $c_0$ ) is generally small (on the order of  $10^{-2}$  or less); this indicates that the model is generally consistent with an offset of zero. However, the added degree of freedom is useful in constraining the data, so setting  $c_0 = 0$  is not endorsed here. The nonlinear term is also very small (on the order of  $10^{-8}$  or less), which indicates that the instrument has a very linear response to the input radiance. The linear term ( $c_1$ ) is dominant for the thermal bands. Note that the LWIR gains are up to 10 % lower when the focal plane temperatures are elevated to 82.5 K.

The calibration coefficients are plotted versus detector for all high gain bands in Figures 7 – 12 for both electronics side (~79.5 K cold focal plane temperatures). Note that the HAM sides are generally very consistent. In addition, there is some odd – even dependence in the gains particularly for bands M13. Also, the gains tend to decrease with detector number for the LWIR bands (I5, M14 – M16).

The mean calibration coefficients for M13 low gain are also listed in Tables 5 – 7. In addition, the M13 low gain coefficients are plotted versus detector in Figures 13 and 14. Note that  $c_0$  is consistently positive, on the order of 0.1 – 0.4. Also, the gain is much lower than the high gain bands ( $1/c_1 \sim 7.7$ ); this is necessary in order for M13 to access scene temperatures up to ~634 K without saturating. Even though the gain is very low, the linear term still dominates ( $c_2 \sim 10^{-7}$ ), indicating that the response is very linear with input radiance.

#### 3.2 Specifications and Sensitivity

Table 8 shows the band average NEdT at  $T_{\text{TYP}}$  for all the thermal bands (HAM A) along with their corresponding requirement. Band M16 does not meet the specification on either electronics side and M15 does not meet the requirement on A side (at the nominal focal plane temperature of 79.5 K). Due to limitations in the test, the SNR fits determined for these two bands need to be extrapolated to  $L_{\text{TYP}}$ .

Better determination of the NEdT is expected in thermal vacuum testing. The high gain NEdT at  $T_{TYP}$  are shown as a function of detector in Figures 15 – 17 (the red dashed line indicates the requirement). Detector 16 in M14 is out-of-family and slightly above the specification for M14 on B side electronics and detector 14 in I5 is out-of-family on A side electronics (at both focal plane temperatures).

The RRCU for each detector are plotted in Figures 18 – 20 along with the requirement (0.001) indicated by the red dashed line. Most bands and detectors fail this specification; however, the higher level specifications that also depend heavily on the radiometric fitting (which are discussed below) generally meet their respective requirements. This indicates that this specification is too strict; a waiver was authorized by the instrument vendor for similar performance on SNPP VIIRS.

Figures 21 – 23 graph the RRNL versus detector for all high gain bands (with a red dashed line for the specification of 0.01). The non-linearity is very consistent over detectors, HAM sides, and electronics sides. All bands pass this requirement.

The worst case detector ARD are graphed in Figures 24 – 26 for all bands. The ARD for all bands is less than 0.2 % above 290 K at a focal plane temperature of 79.5 K and below 0.4 % at 82.5 K; this indicates that the fitting contribution to the radiance retrieval is accurate for these bands. The MWIR bands are known to exhibit non-linear behavior, especially below 270 K; however, this behavior will not be visible until thermal vacuum measurements are made using lower source temperatures. All bands are well within their specified limits.

Figures 27 – 29 show the worst case detector RRU for all high gain bands within the specified temperature range (between  $L_{MIN}$  and  $0.9L_{MAX}$ ). The RRU is within the specifications for A side electronics at both focal plane temperatures; however, the RRU is greater than one for M13, M14, and M16B at selected scene temperature for electronics side B (due to the shift in the focal plane temperatures). The RRU is essentially a measure of detector to detector uniformity in the retrieved radiance in relation to the NEdL, which is an indicator of whether the striping is within the noise resolution.

The band average saturation temperatures are listed in Table 9 for both electronics sides (HAM side A). All bands exceed the specified upper limit ( $T_{MAX}$ ) except I4. The response of both I4 and M12 rolls over at scene temperatures not far above the true saturation temperatures. This causes sharp edges as the telescope scans the source profile which make the saturation determination difficult. Thermal vacuum test data should provide better results and it is expected that I4 will meet this requirement. All other thermal bands digitally saturate first and roll over is not observed for the scene temperatures measured. In addition, it was observed that M15 detector 1 saturated earlier than the other detectors (at about 345 K), but was still above the specified  $T_{MAX}$ .

The quantities associated with these specifications (NEdT at  $T_{TYP}$ , RRNL, RRCU, ARD, and RRU) were also calculated for M13 low gain. The band average NEdT at  $T_{TYP}$  for M13 low gain is shown in Table 8; all detectors are well below the specification. The RRCU is about 0.01 (which exceeds the specification) and the RRNL is below  $\sim 0.002$ . This indicates that M13 low gain is very linear in its response and that the fitting residual is small. In addition, the worst case retrieval error (ARD) is less than  $\sim 2.0$  % at the low end of the dynamic range and less than 1.0 % above 450 K. The worst case detector uniformity is below the detector resolution over the specified range.

#### 4. Summary

RC-1 part 1 data was analyzed under ambient conditions for the VIIRS F2 sensor. Radiometric coefficients were determined for all thermal bands, detectors, HAM and electronics sides. Analysis showed the following:

- Radiometric fitting dominated by linear term. Offsets and nonlinear terms are small on the order of 0.01 and  $10^{-8}$  respectively.
- Radiometric gains decreased ~10 % for LWIR bands when the cold focal plane temperatures increased from ~79.5 to 82.5 K. MWIR band gains were comparable.
- Dynamic range requirement was met in terms of saturation for all thermal bands except I4. Roll over in I4 response made determination difficult and it is expected that thermal vacuum data will show I4 in compliance. In addition, detector 1 in band M15 saturated about 15 K lower than the other detectors, but still above  $T_{MAX}$ .
- The sensitivity of the thermal bands was measured in terms of their NEdT at  $T_{TYP}$ , which was within the specified limits for most bands. The test required extrapolation to  $T_{TYP}$  for bands M15 and M16, and both these bands exceed the specification; thermal vacuum data is expected to show these bands in compliance.
- Response nonlinearity was shown to be in compliance for all bands.
- Characterization uncertainty was shown to be in non-compliance for almost all bands and detectors. Improved results are expected using thermal vacuum data, but this requirement remains challenging as was observed with SNPP VIIRS.
- All bands were within the absolute radiometric calibration in terms of the measure ARD over the scene temperatures measured.
- Detector to detector striping was generally within the noise with some exceptions on electronic side B. Results are expected to improve using thermal vacuum data.

Table 1: Data used in RC-1 part 1 analysis (electronics side A). Low temperature collects 1 and 2 are nominal and 60 % integration time using the M16A DPP & APID band substitution table and collects 3 and 4 are nominal and 60 % integration time using the Default DPP & M16B APID band substitution table. High temperature collects 1 and 2 are nominal and 60 % integration time in fixed high gain using the M16A DPP & APID band substitution table, collects 3 and 4 are nominal and 60 % integration time in fixed low gain using the Default DPP & M16B APID band substitution table, and collects 5 and 6 are nominal and 60 % integration time in auto gain using the Default DPP & M16B APID band substitution table. The cold focal planes were controlled at 79.5 K.

UAID	Collects	LABB T [K]	TMC BB [K]	OBC BB [K]
4300910	1-4	293	295	294
4300911	1-4	298	300	294
4300912	1-4	303	306	294
4300913	1-4	308	313	294
4300914	1-4	313	320	294
4300915	1-4	318	326	294
4300916	1-4	323	333	294
4300917	1-4	328	340	294
4300918	1-4	333	346	294
4300919	1-4	338	353	294
4300920	1-4	345	363	294
4300921	2-7	345	393	294
4300922	1-6	345	413	294
4300923	1-6	345	428	294
4300924	1-6	345	523	294
4300925	1-6	345	578	294
4300926	1-6	345	638	294
4300927	1-6	345	693	294
4300928	1-6	345	748	294

Table 2: Data used in RC-1 part 1 analysis (electronics side B). Low temperature collects 1 and 2 are nominal and 60 % integration time using the M16A DPP & APID band substitution table and collects 3 and 4 are nominal and 60 % integration time using the Default DPP & M16B APID band substitution table. High temperature collects 1 and 2 are nominal and 60 % integration time in fixed high gain using the M16A DPP & APID band substitution table, collects 3 and 4 are nominal and 60 % integration time in fixed low gain using the Default DPP & M16B APID band substitution table, and collects 5 and 6 are nominal and 60 % integration time in auto gain using the Default DPP & M16B APID band substitution table. The cold focal planes were controlled at 79.5 K.

UAID	Collects	LABB T [K]	TMC BB [K]	OBC BB [K]
4301729	1-4	293	293	294
4301730	1-4	298	300	294
4301731	1-4	303	306	294
4301732	1-4	308	313	294
4301733	1-4	313	320	294
4301734	1-4	318	326	294
4301735	1-4	323	333	294
4301736	1-4	328	340	294
4301737	1-4	333	346	294
4301738	1-4	338	353	294
4301739	1-4	345	363	294
4301740	1-6	345	393	294
4301741	1-6	345	413	294
4301742	1-6	345	428	294
4301743	1-6	345	523	294
4301744	1-6	345	578	294
4301745	1-6	345	638	294
4301746	1-6	345	673	294
4301747	1-6	345	748	294

Table 3: Data used in ETP-249 analysis (electronics side A). Low temperature collects 1 and 2 are nominal and 60 % integration time. The cold focal planes were controlled at 82.5 K.

UAID	Collects	LABB T [K]	TMC BB [K]	OBC BB [K]
4301001	1-2	293	295	294
4301002	1-2	298	300	294
4301003	1-2	303	306	294
4301004	1-2	308	313	294
4301005	1-2	313	320	294
4301006	1-2	318	326	294
4301007	1-2	323	333	294
4301008	1-2	328	340	294
4301009	1-2	333	346	294
4301010	1-2	338	353	294
4301011	1-2	345	363	294

Table 4: Sample ranges used for data analysis. Saturation analysis was performed only with TMC BB data and used a wider sample range.

Test	Band Type	Analysis	LABB	TMC BB
RC-1 part 1	M single	Normal	1035—1109	2125—2139
	M dual		1457—1679	4727—4769
	I		2070—2219	4250—4279
	M single	Saturation		2120—2149
	M dual			4712—4799
	I			4240—4299
ETP-249	M	Normal	880—1129	
	I		1760—2259	

Table 5: band average thermal band  $c_0$  (HAM side A).

Band	A side	B side	ETP-249
I4	0.0022	0.00012	-0.0020
I5	0.012	0.0019	-0.022
M12	0.0017	-0.00017	-0.0020
M13 HG	0.0025	-0.00096	-0.0046
M13 LG	0.26	0.21	~
M14	0.013	0.021	-0.035
M15	0.016	0.011	-0.024
M16A	0.0087	0.015	-0.022
M16B	0.013	0.022	-0.022

Table 6: band average thermal band gains ( $1/c_1$ ) (HAM side A).

Band	A side	B side	ETP-249
I4	1147	1135	1146
I5	185	181	163
M12	1154	1139	1154
M13 HG	607	600	606
M13 LG	7.7	7.7	~
M14	190	184	163
M15	193	188	180
M16A	202	198	181
M16B	202	198	180

Table 7: band average thermal band  $c_2$  (HAM side A).

Band	A side	B side	ETP-249
I4	-3.3e-9	-6.8e-9	-2.1e-9
I5	-1.9e-8	6.9e-10	1.1e-9
M12	-5.0e-9	-8.8e-9	-3.8e-9
M13 HG	-1.2e-8	-1.9e-8	-9.9e-9
M13 LG	-5.0e-7	-5.3e-7	~
M14	1.5e-8	3.5e-8	5.5e-8
M15	-1.2e-8	-1.6e-8	5.7e-9
M16A	-1.3e-8	4.5e-9	6.9e-9
M16B	-4.1e-9	1.7e-8	7.5e-9

Table 8: band averaged NEdT at  $T_{TYP}$  [K] for HAM A compared to the specification [2].

Band	A side	B side	ETP-249	Specification
I4	0.562	0.620	0.548	2.5
I5	0.488	0.481	0.518	1.5
M12	0.199	0.207	0.175	0.396
M13 HG	0.056	0.056	0.057	0.107
M13 LG	0.265	0.289	~	0.423
M14	0.070	0.071	0.066	0.091
M15	0.084	0.047	0.060	0.072
M16A	0.101	0.099	0.084	0.070
M16B	0.111	0.099	0.086	0.070

Table 9: band average saturation temperature [K] for HAM A compared to specified  $T_{MAX}$  [2].

Band	A side	B side	$T_{MAX}$
I4	349	350	353
I5	371	375	340
M12	357	357	353
M13 HG	351	351	343
M13 LG	659	660	634
M14	349	353	336
M15	358	360	343
M16A	369	372	340
M16B	370	374	340

Figure 1: at-detector radiance versus dn for all high gain bands, HAM side A and electronics side A.

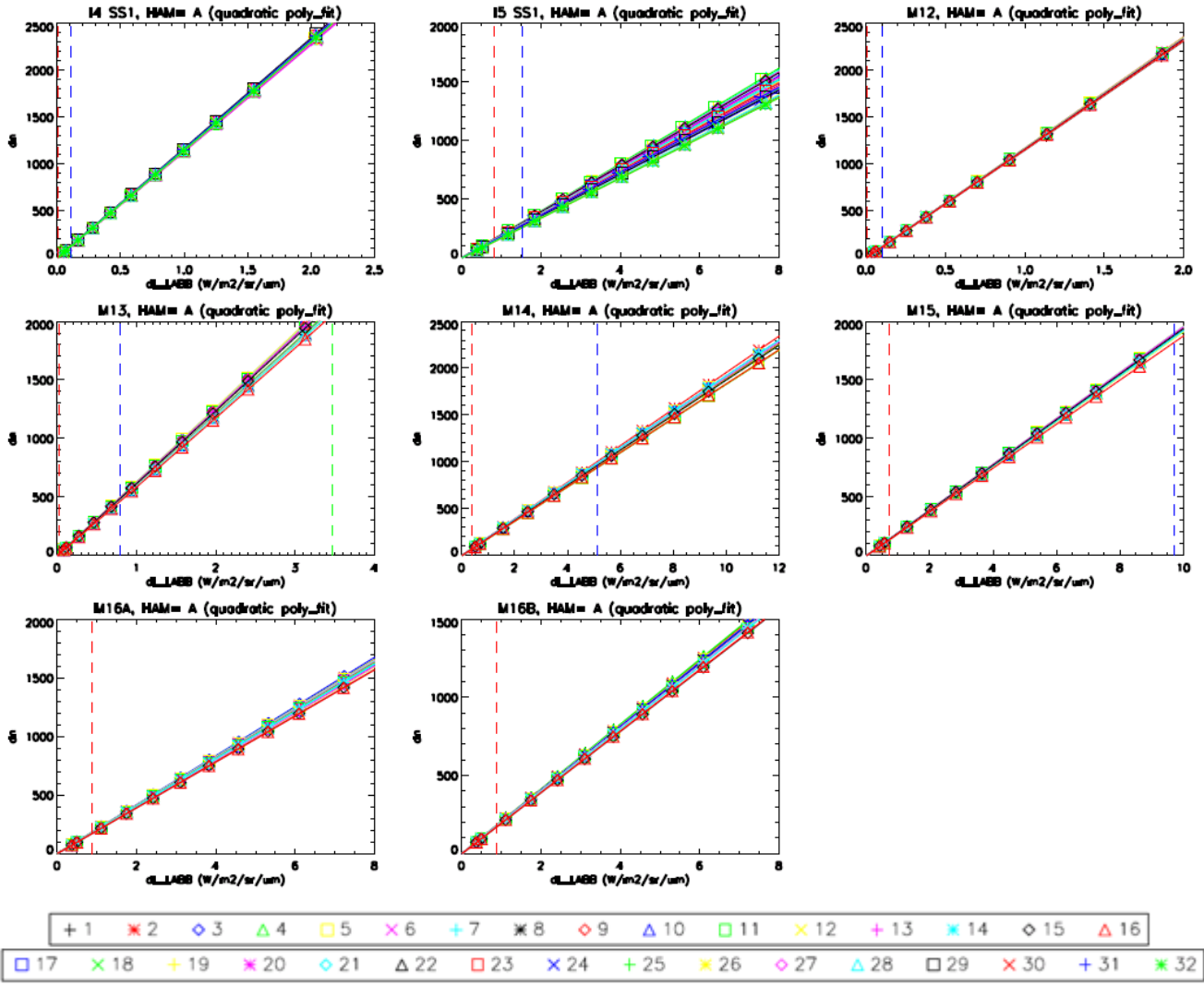


Figure 2: radiance residuals versus at-detector radiance for all high gain bands, HAM side A and electronics side A.

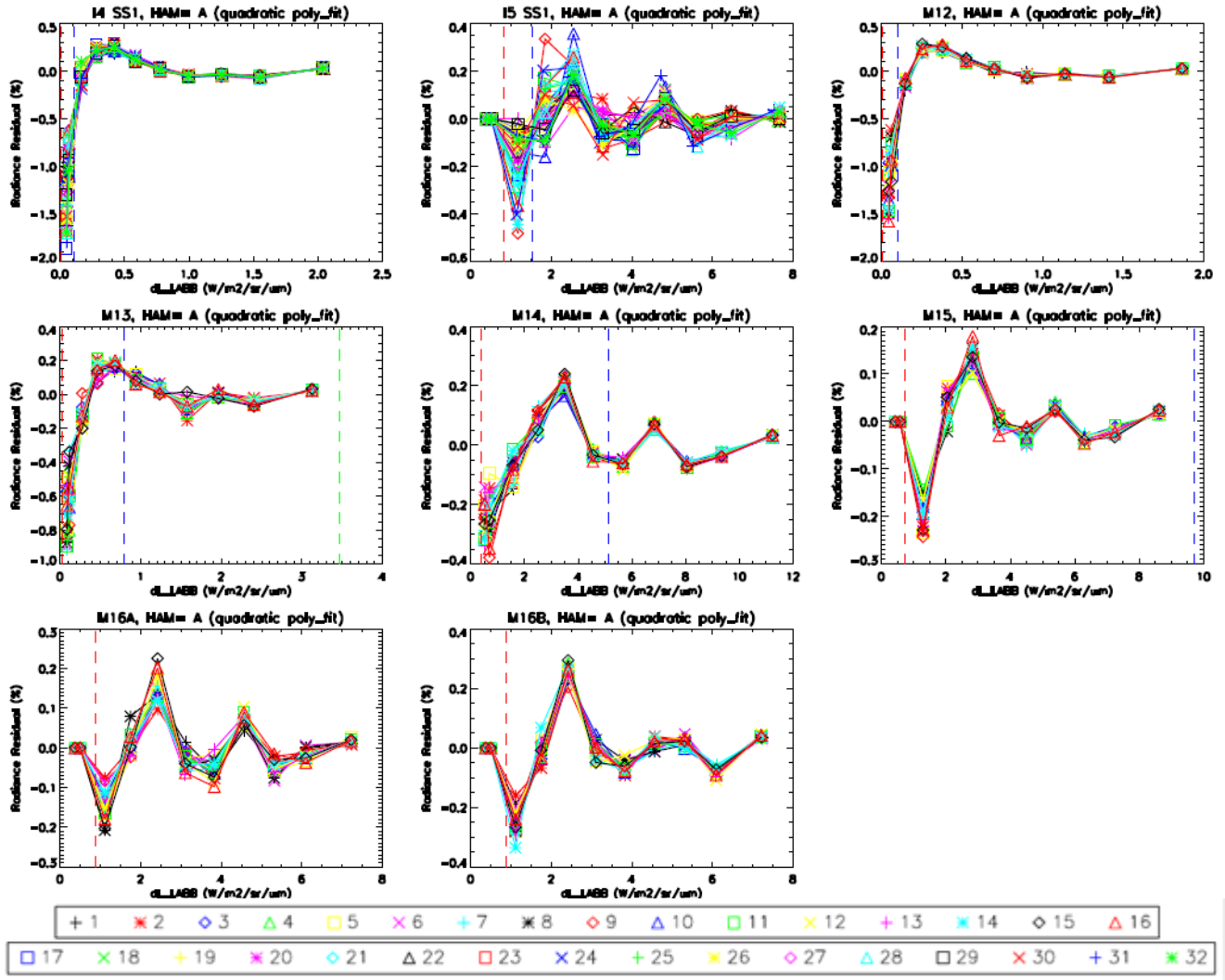


Figure 3: at-detector radiance versus dn for all high gain bands, HAM side A and electronics side B.

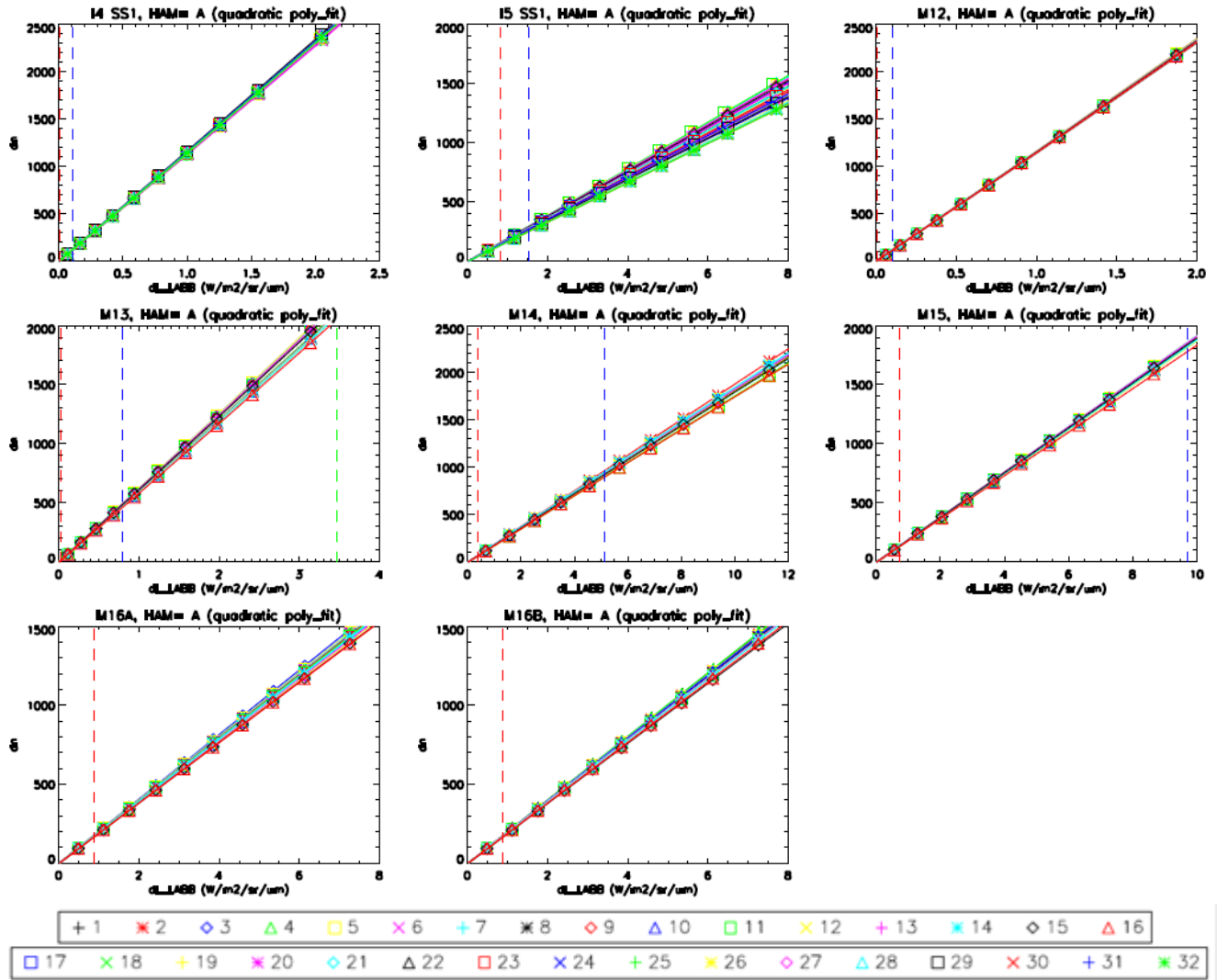


Figure 4: radiance residuals versus at-detector radiance for all high gain bands, HAM side A and electronics side A.

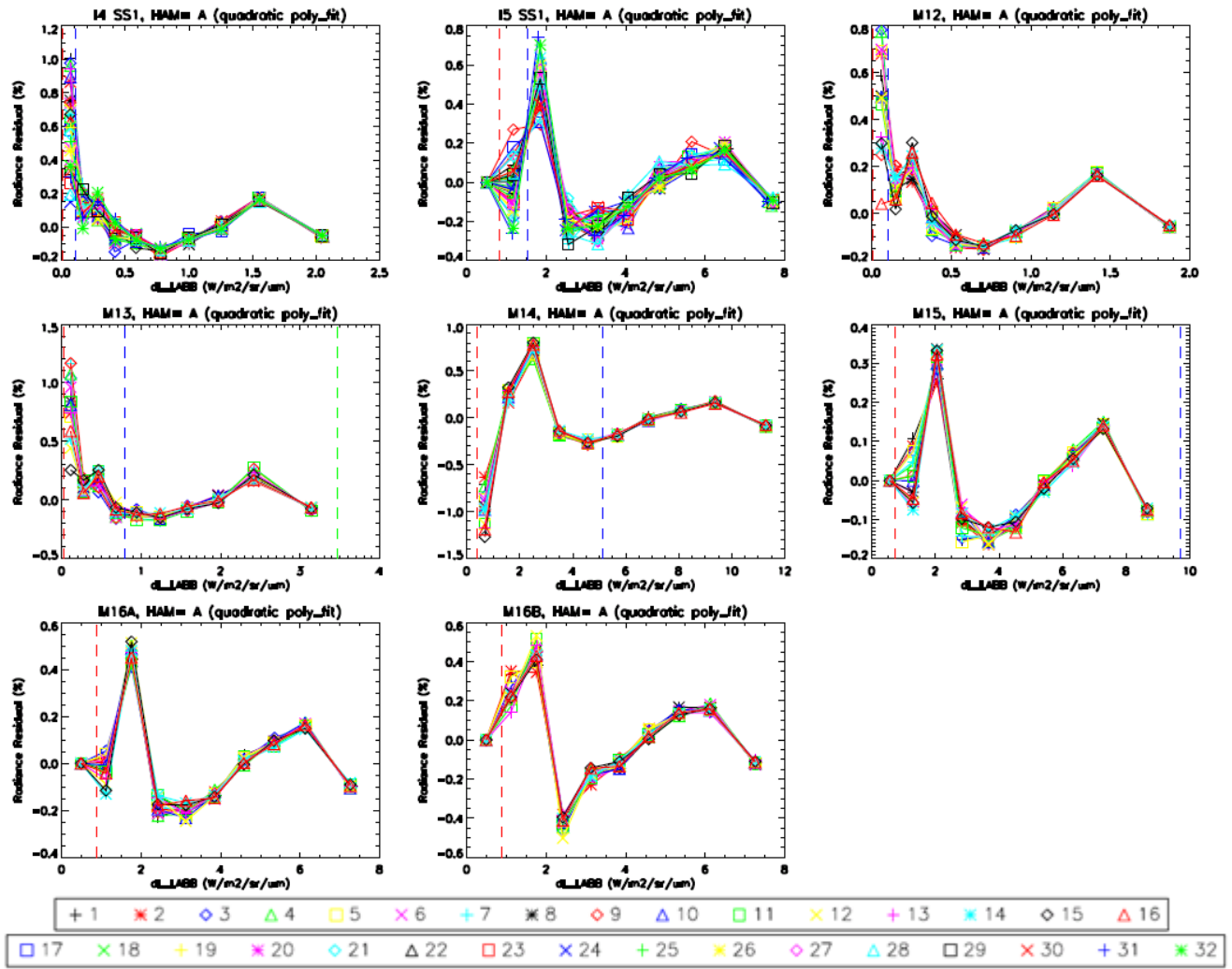


Figure 5: at-detector radiance versus dn for all high gain bands, HAM side A and electronics side A (cold focal planes ~82.5 K).

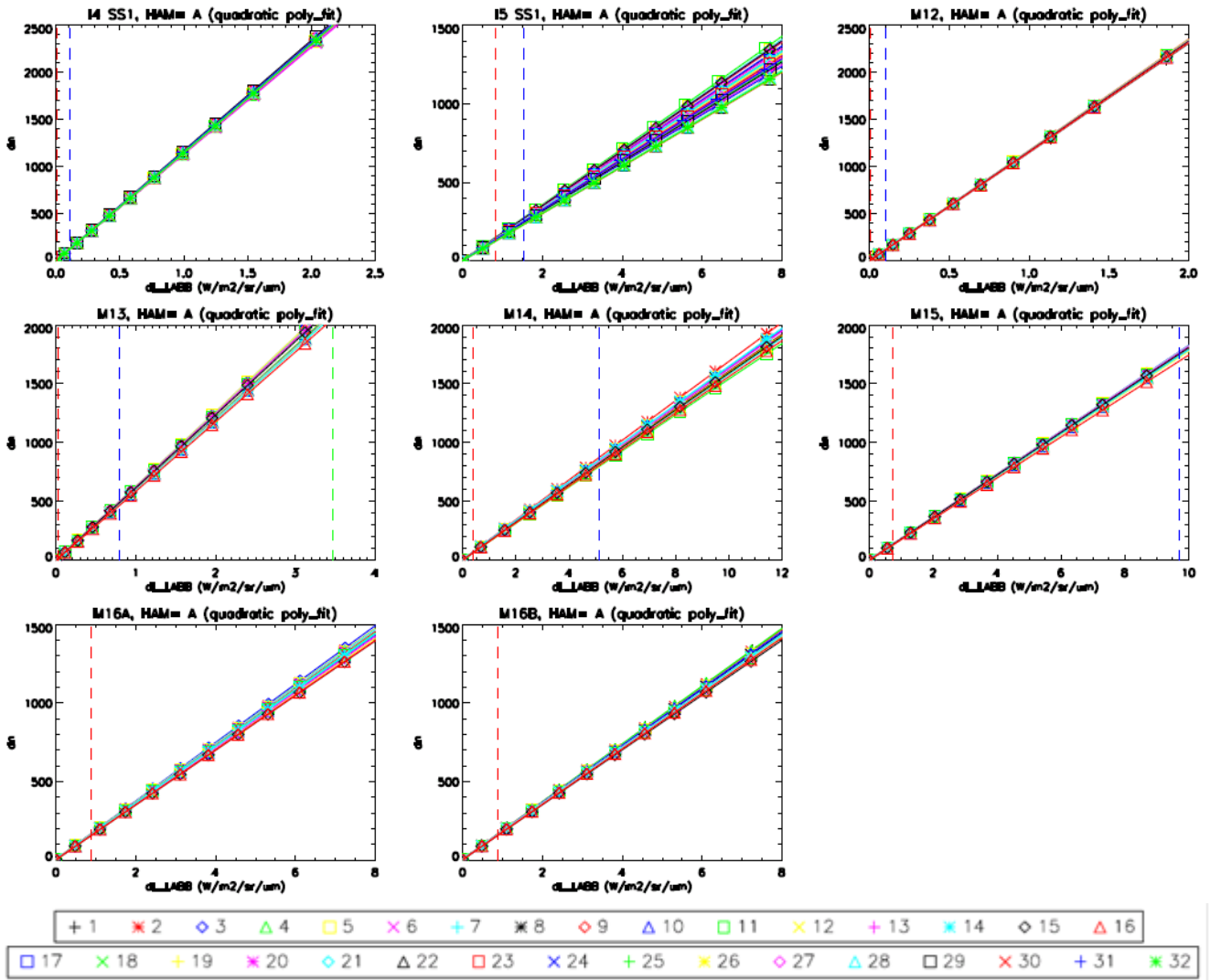


Figure 6: radiance residuals versus at-detector radiance for all high gain bands, HAM side A and electronics side A (cold focal planes ~82.5 K).

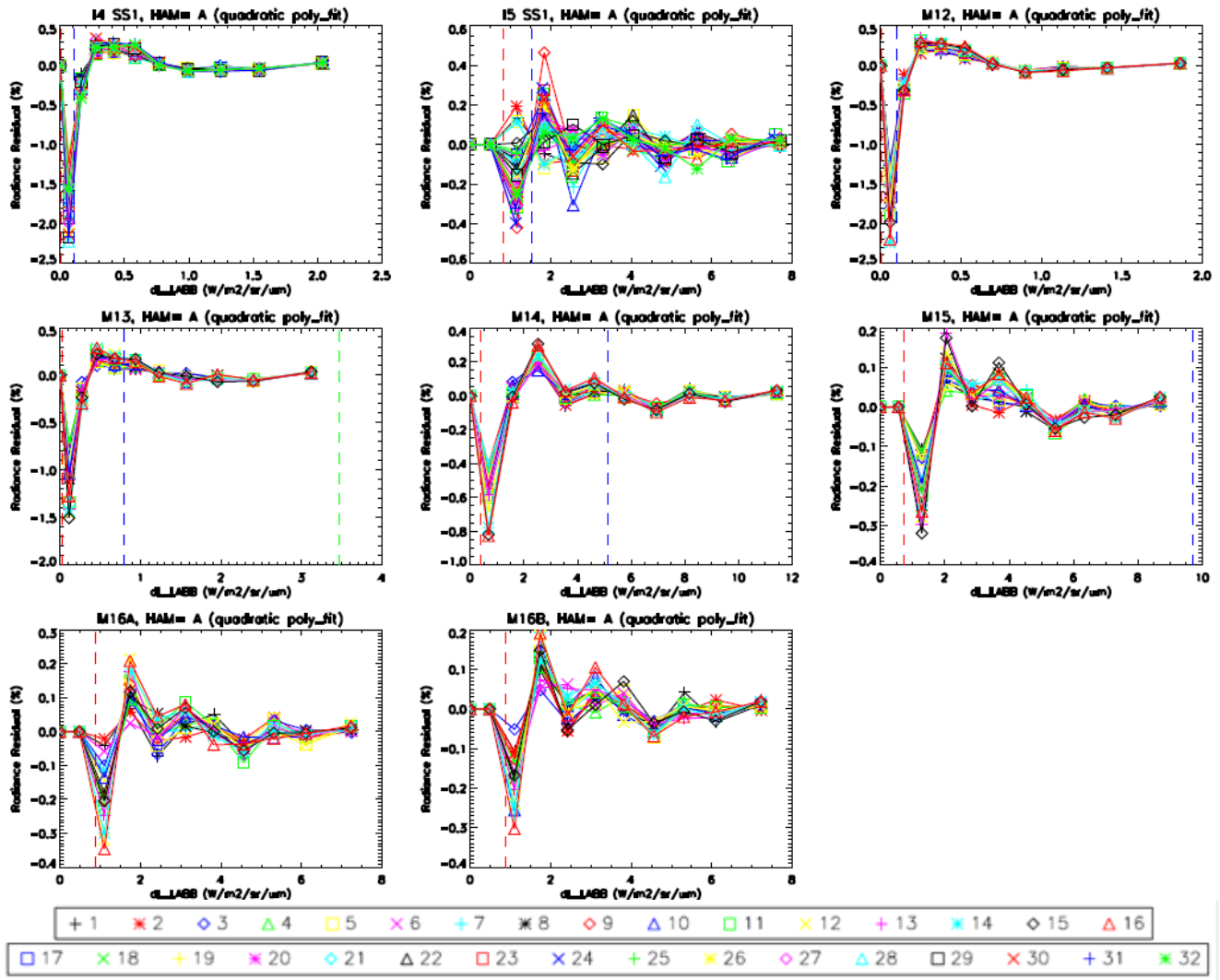


Figure 7:  $c_0$  coefficients for high gain bands (electronics side A).

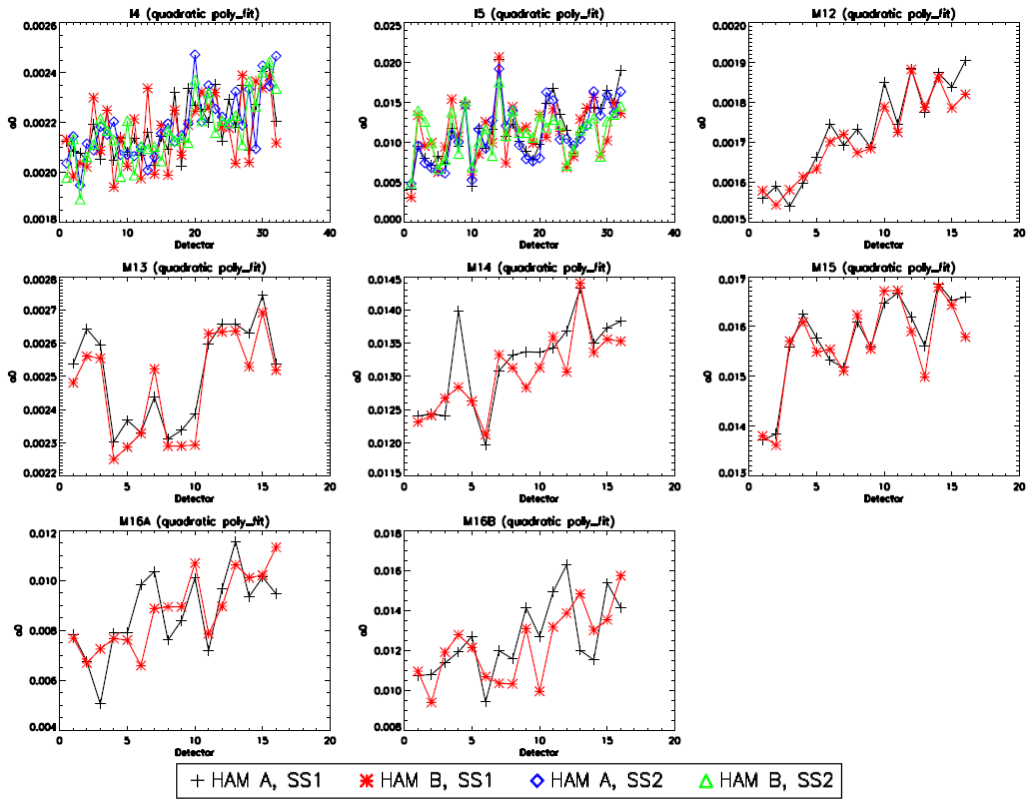


Figure 8:  $c_0$  coefficients for high gain bands (electronics side B).

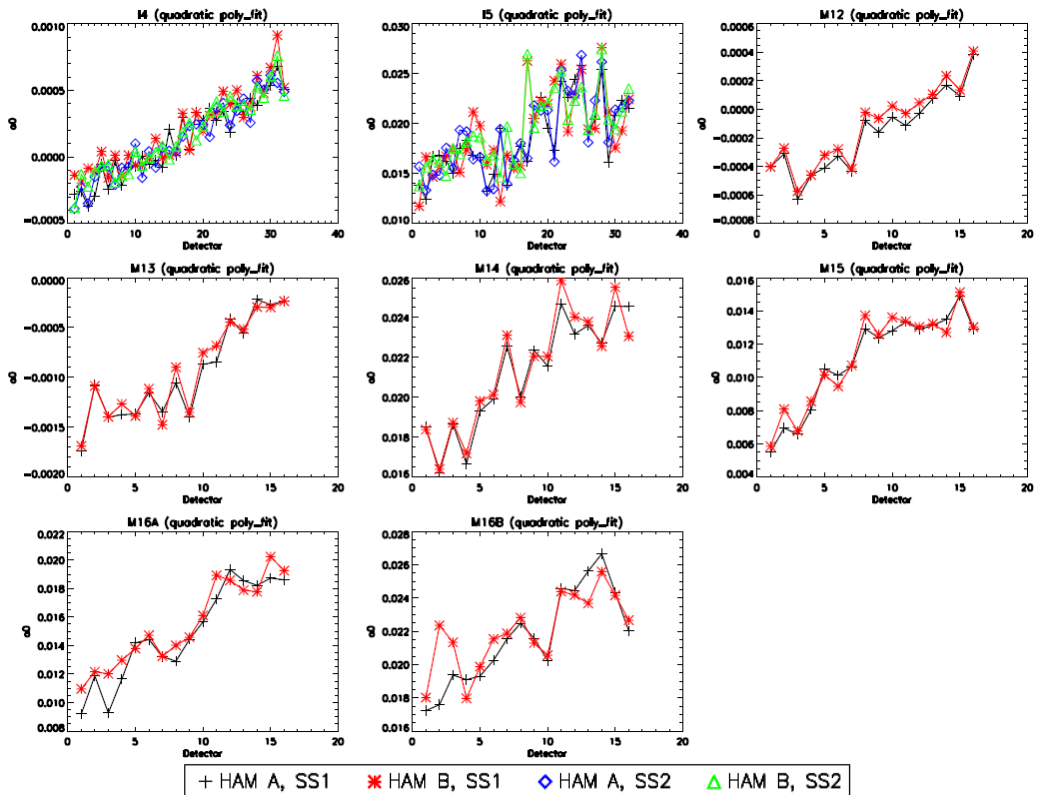


Figure 9:  $1/c_1$  coefficients for high gain bands (electronics side A).

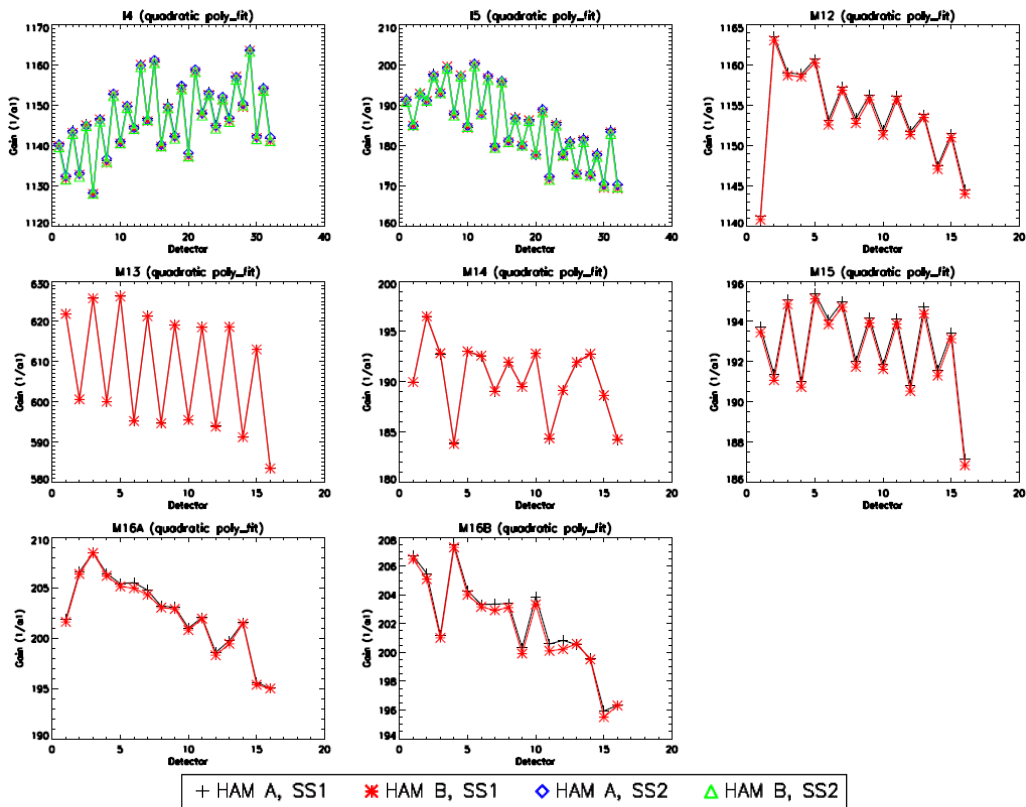


Figure 10:  $1/c_1$  coefficients for high gain bands (electronics side B).

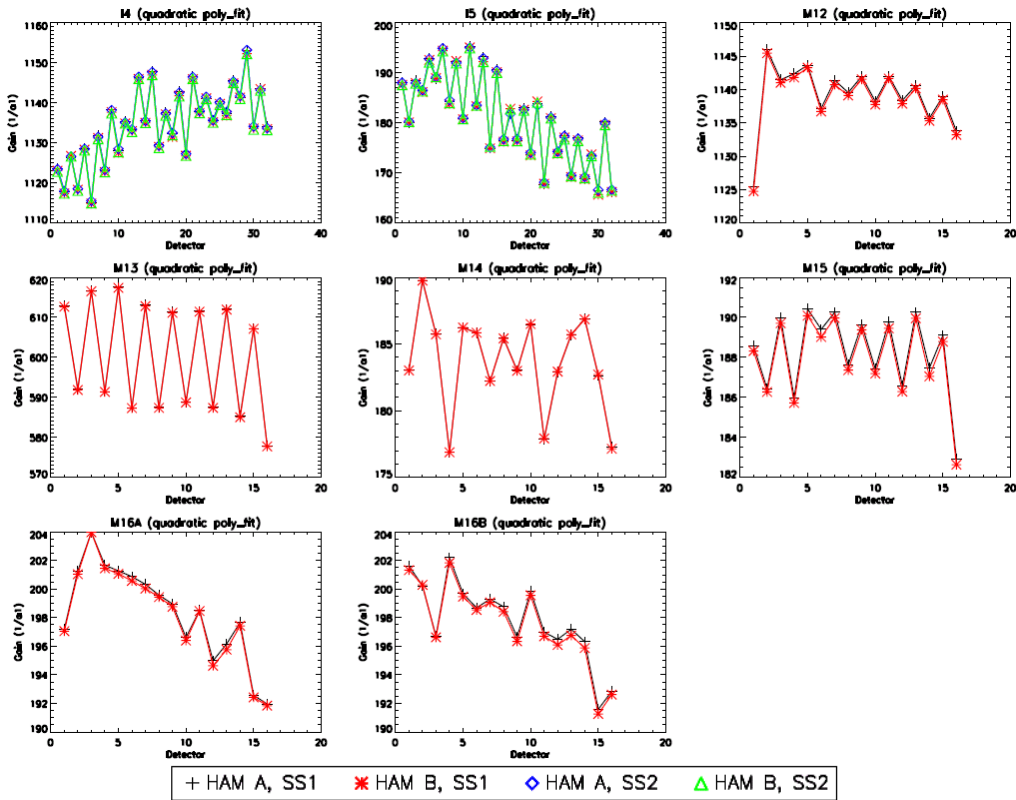


Figure 11:  $c_2$  coefficients for high gain bands (electronics side A).

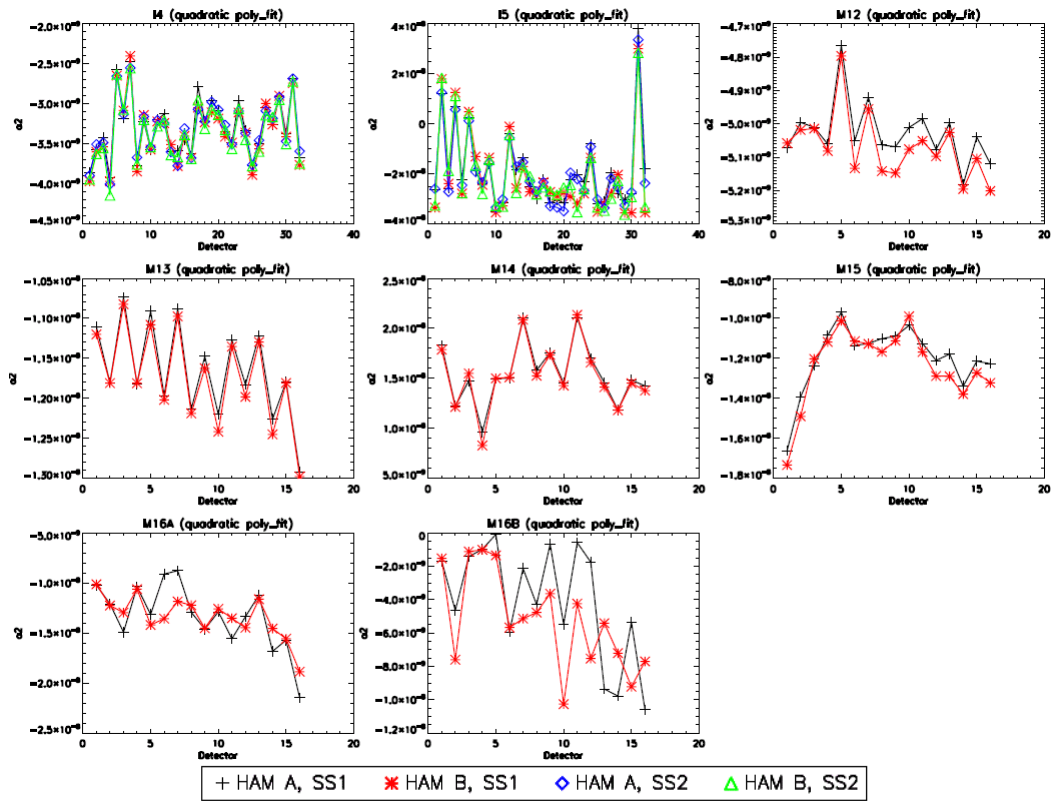


Figure 12:  $c_2$  coefficients for high gain bands (electronics side B).

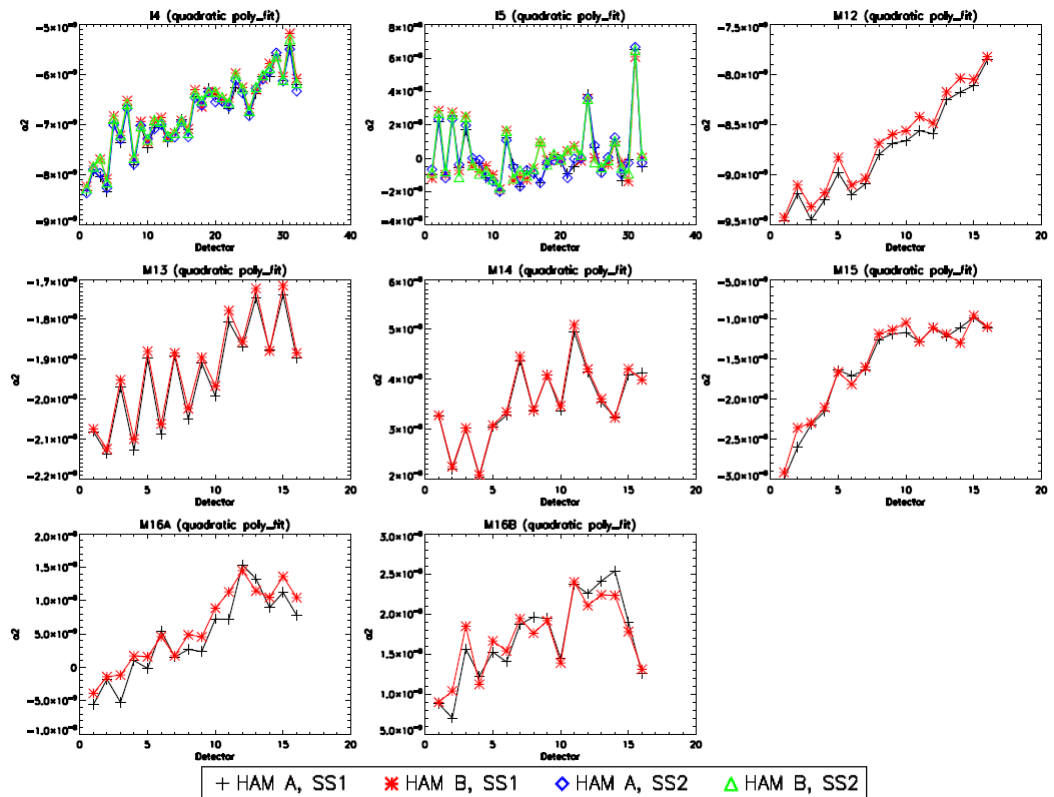


Figure 13: M13 low gain coefficients for electronics side A.

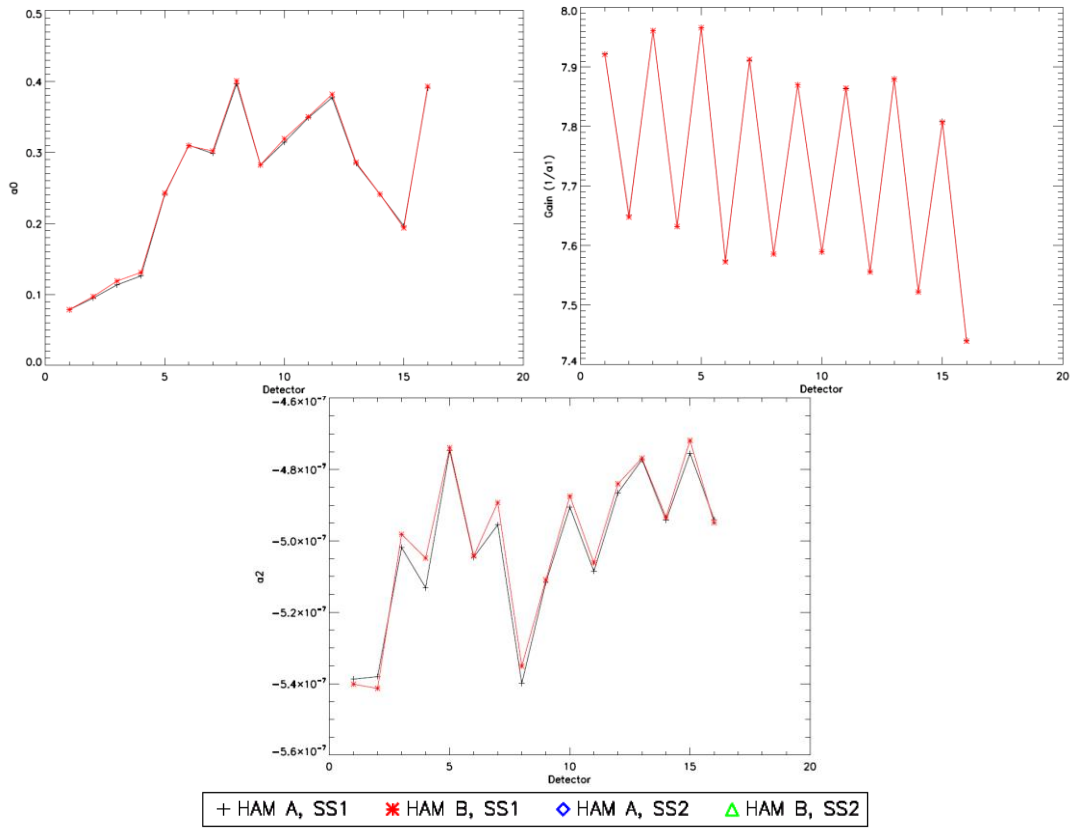


Figure 14: M13 low gain coefficients for electronics side B.

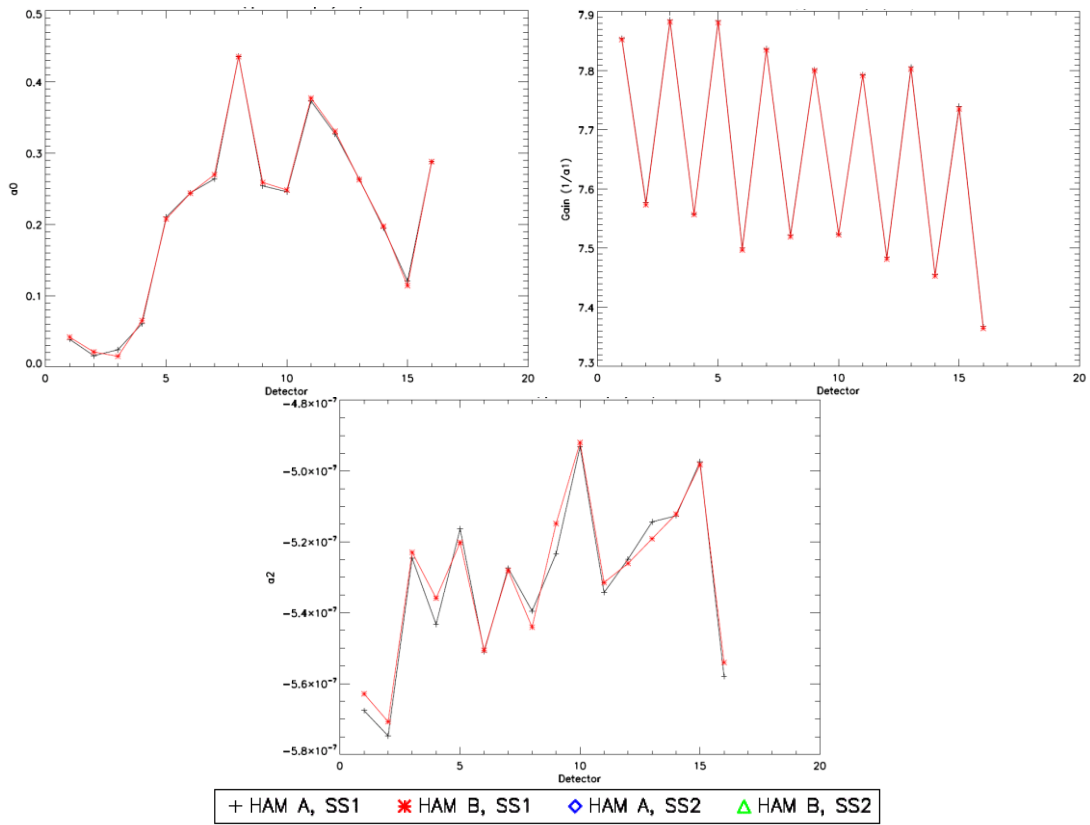


Figure 15: NEdT at  $T_{\text{Typ}}$  versus detector for electronics side A (the red dashed line denotes the specified limit).

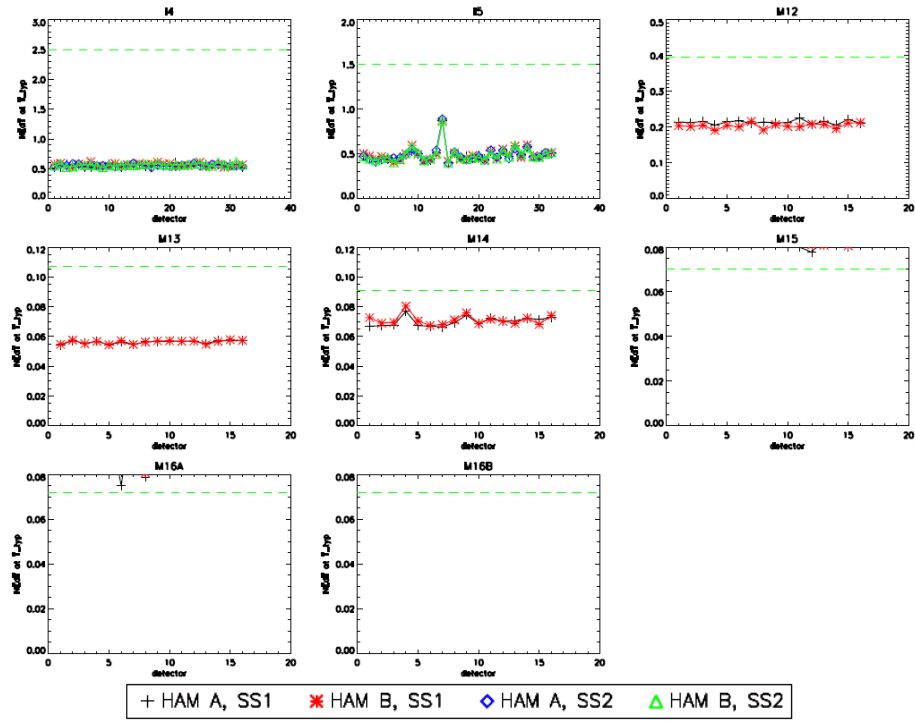


Figure 16: NEdT at  $T_{\text{Typ}}$  versus detector for electronics side B (the red dashed line denotes the specified limit).

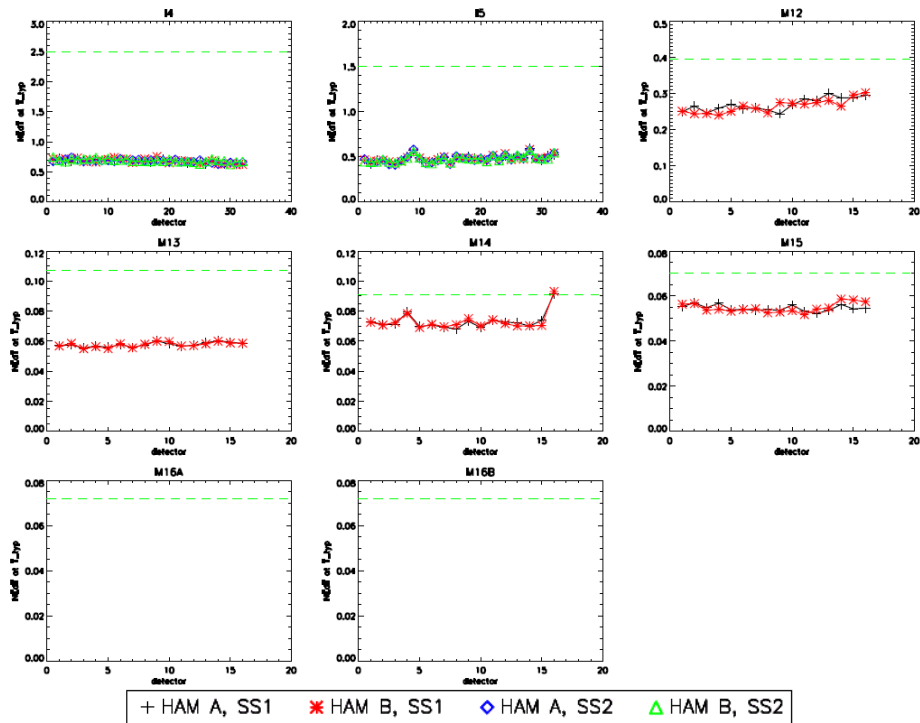


Figure 17: NEdT at  $T_{\text{Typ}}$  versus detector for electronics side A and a cold focal plane temperature of 82.5 K (the red dashed line denotes the specified limit).

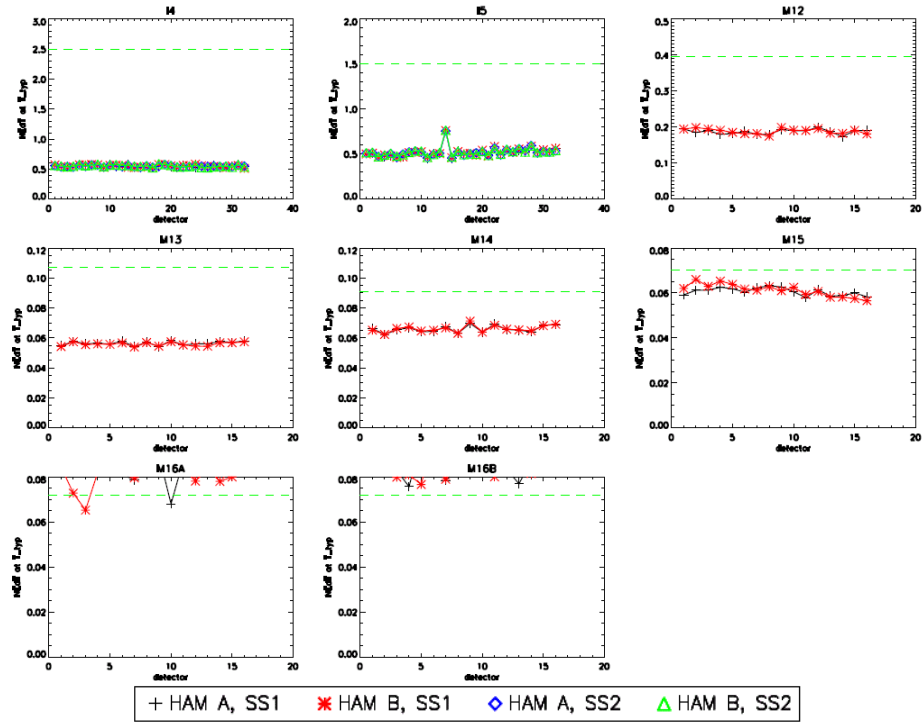


Figure 18: RRCU for high gain bands on electronics side A (the red dashed line denotes the specified limit).

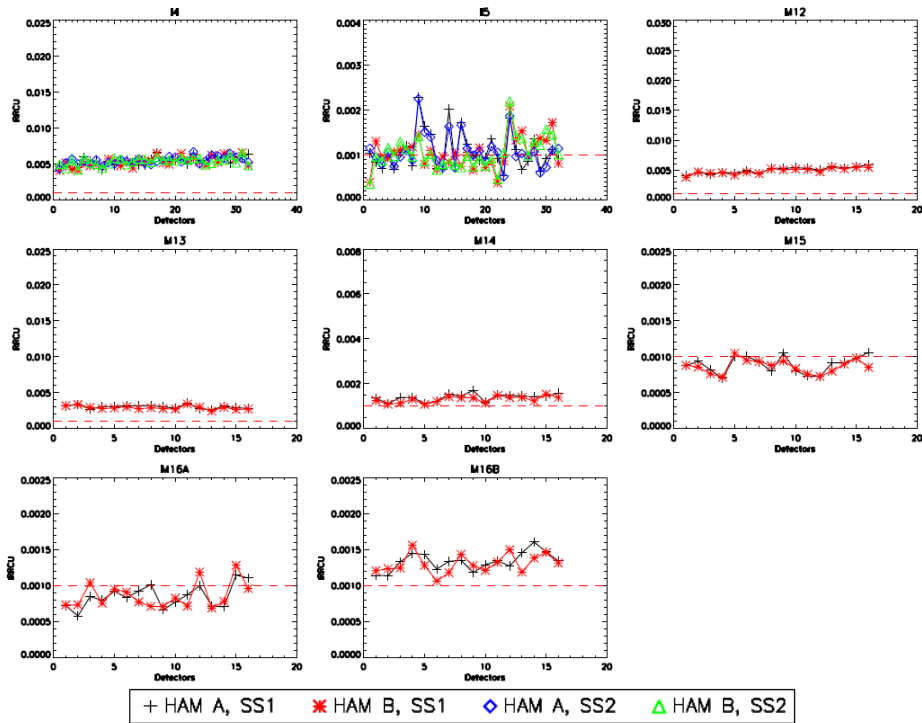


Figure 19: RRCU for high gain bands on electronics side B (the red dashed line denotes the specified limit).

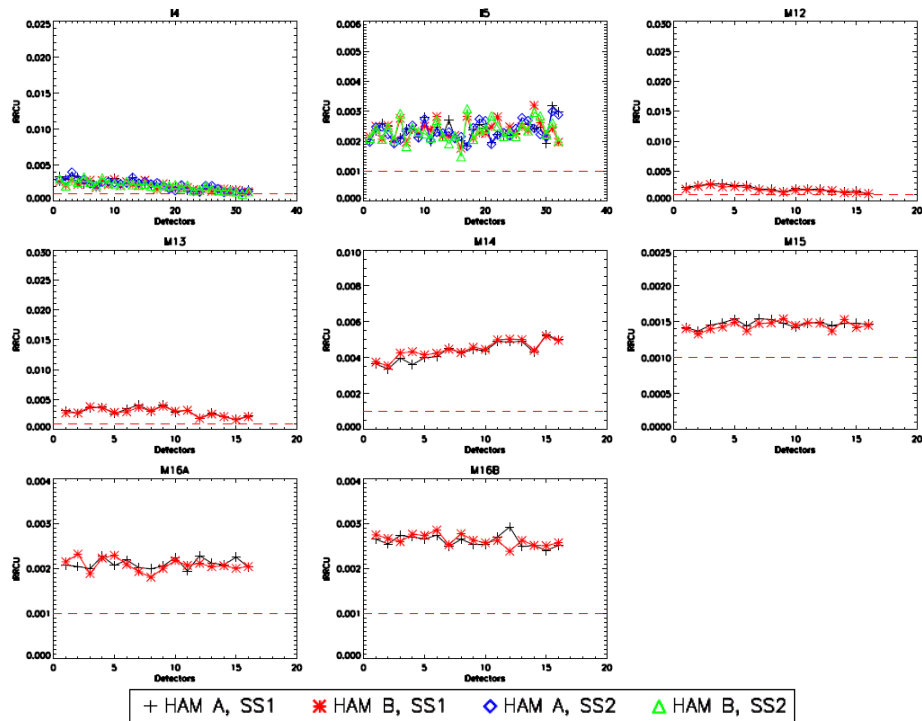


Figure 20: RRCU for high gain bands on electronics side A and a cold focal plane temperature of 82.5 K (the red dashed line denotes the specified limit).

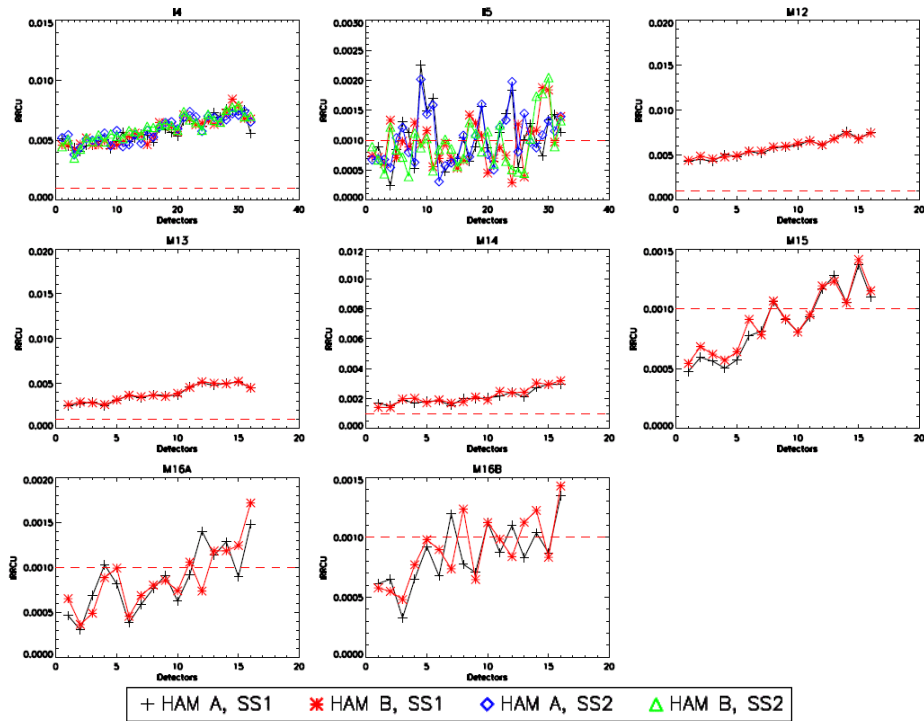


Figure 21: RRNL for high gain bands on electronics side A (the red dashed line denotes the specified limit).

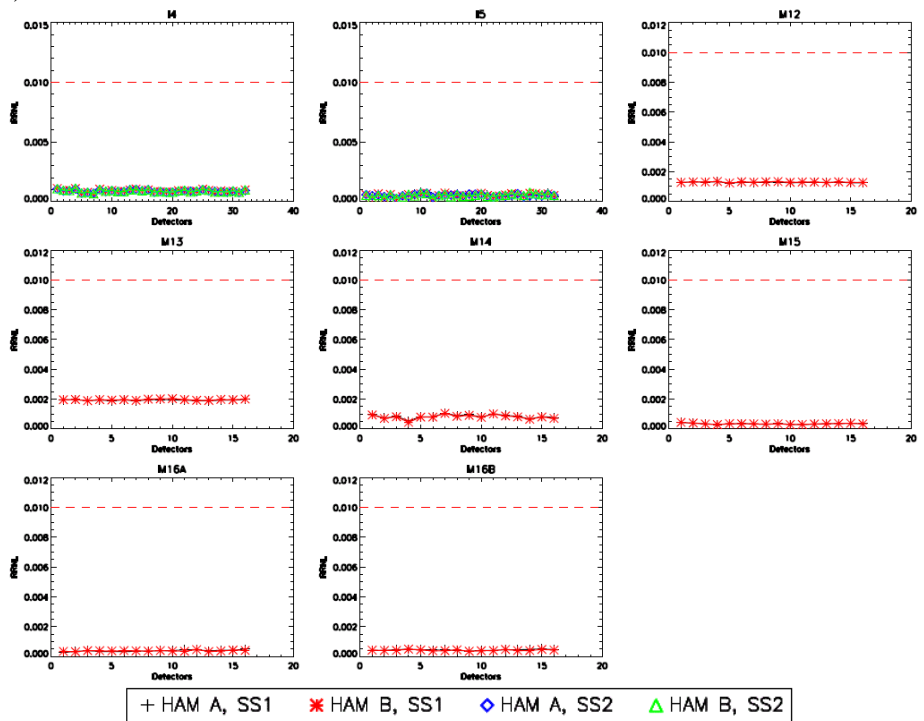


Figure 22: RRNL for high gain bands on electronics side B (the red dashed line denotes the specified limit).

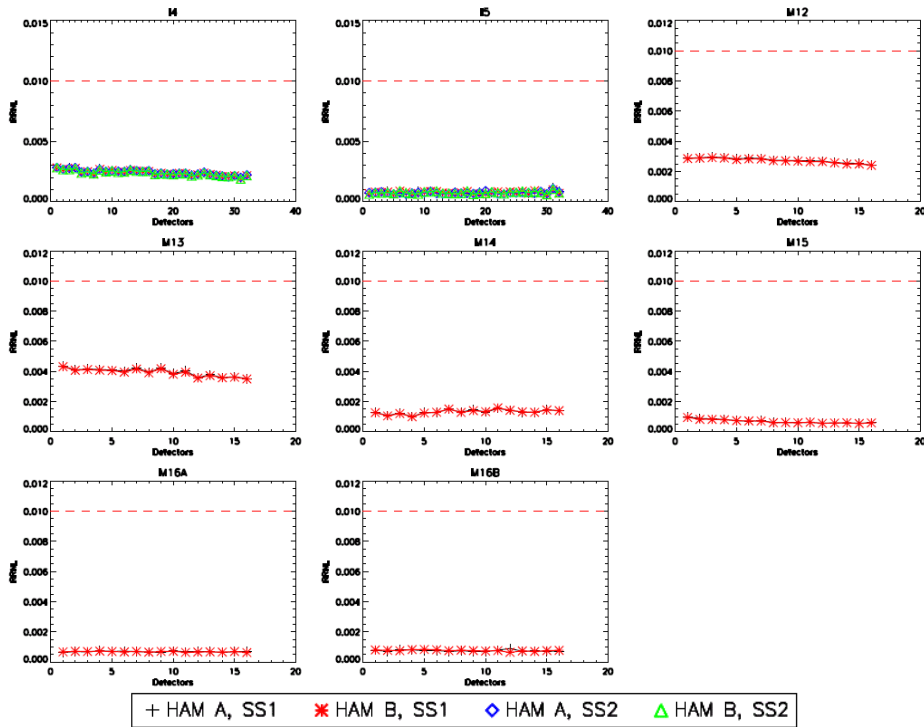


Figure 23: RRNL for high gain bands on electronics side A and a cold focal plane temperature of 82.5 K (the red dashed line denotes the specified limit).

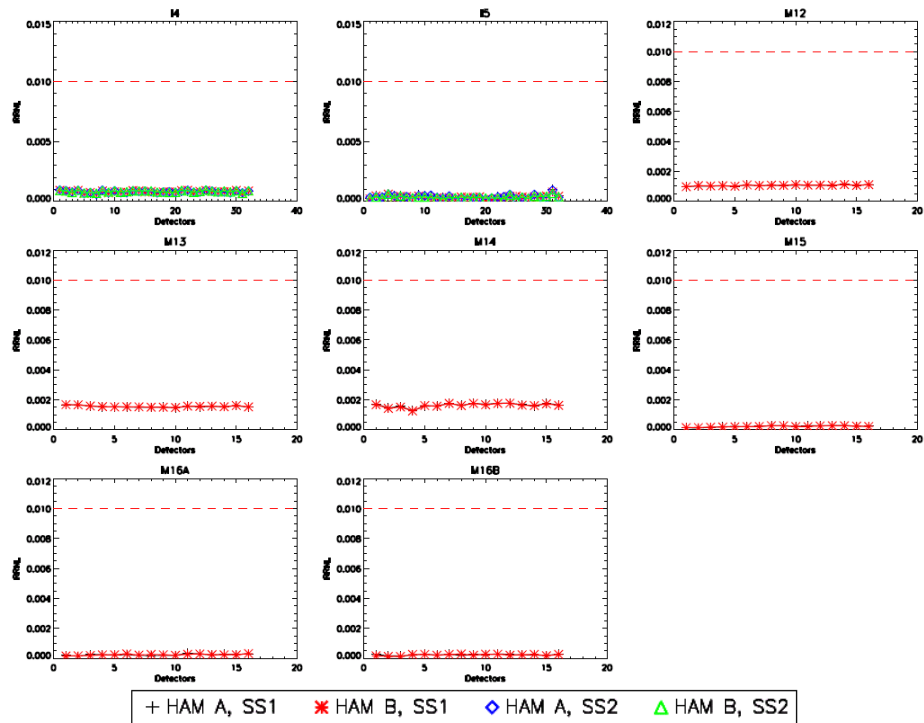




Figure 26: worst case detector ARD versus scene temperature [K] for electronics side A and a cold focal plane temperature of 82.5 K.

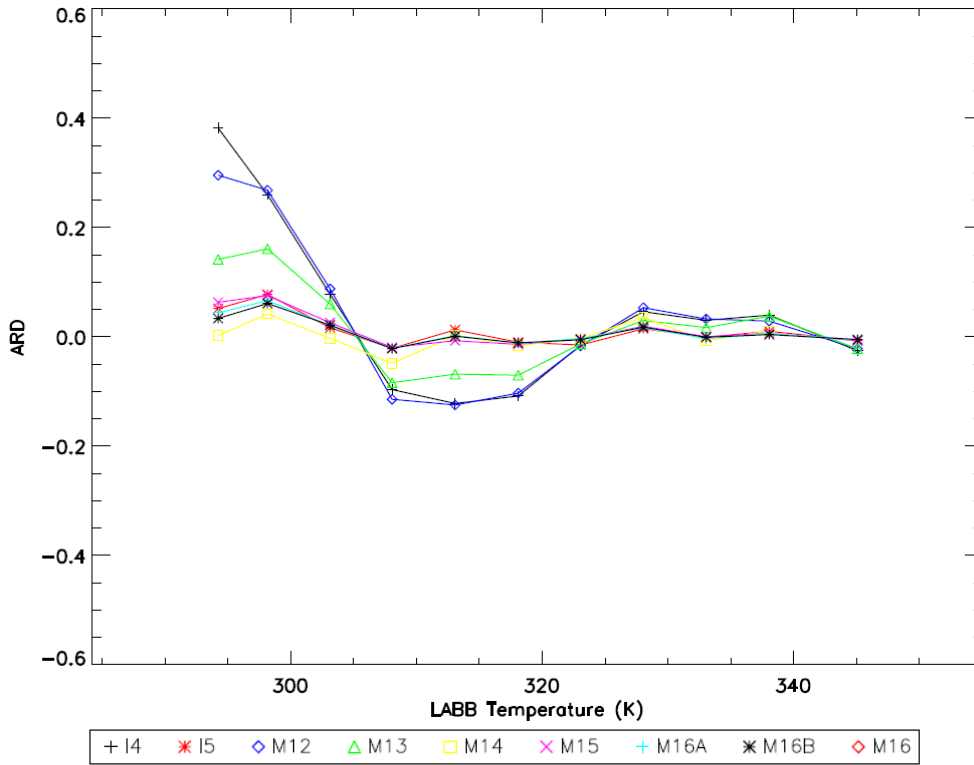


Figure 27: worst case detector RRU versus scene temperature [K] for electronics side A.

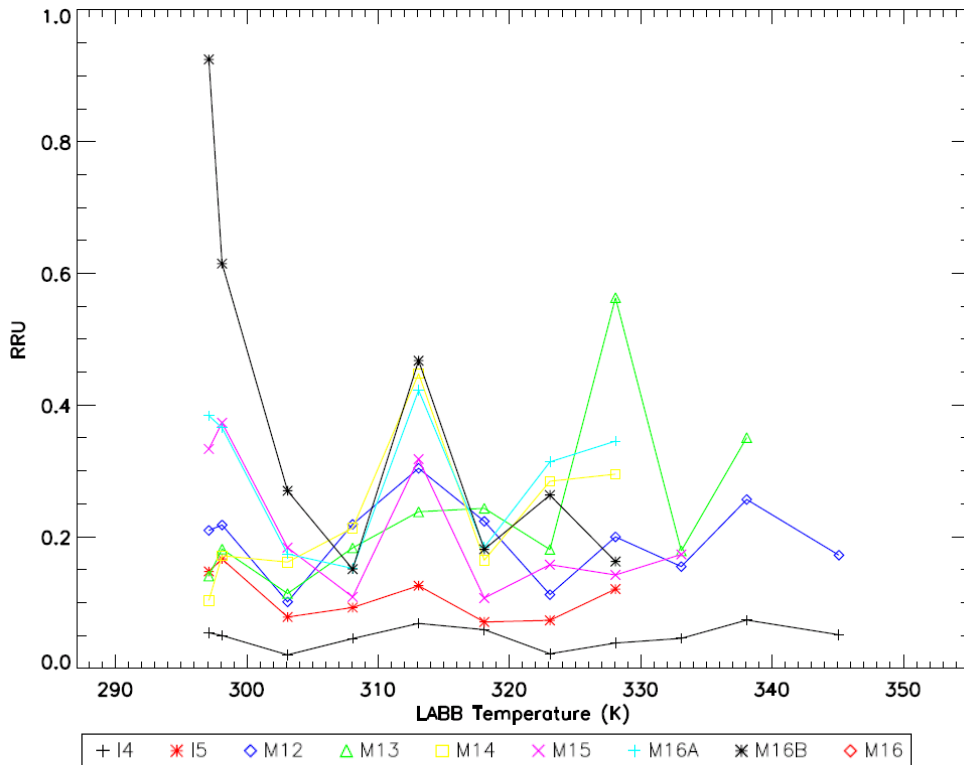


Figure 28: worst case detector RRU versus scene temperature [K] for electronics side B.

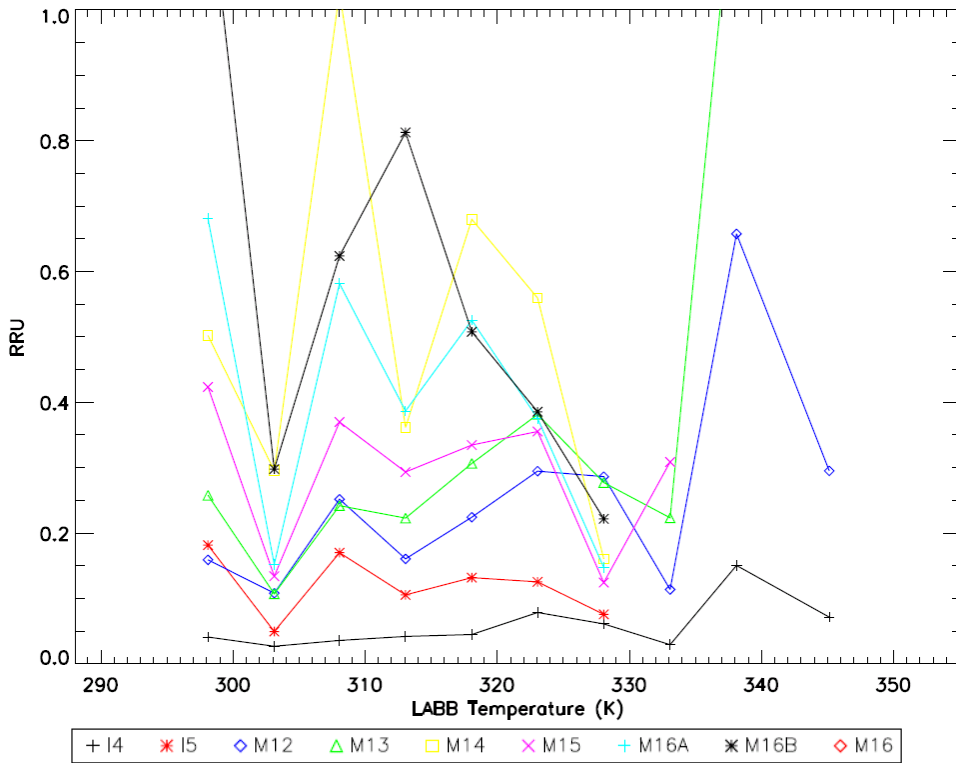
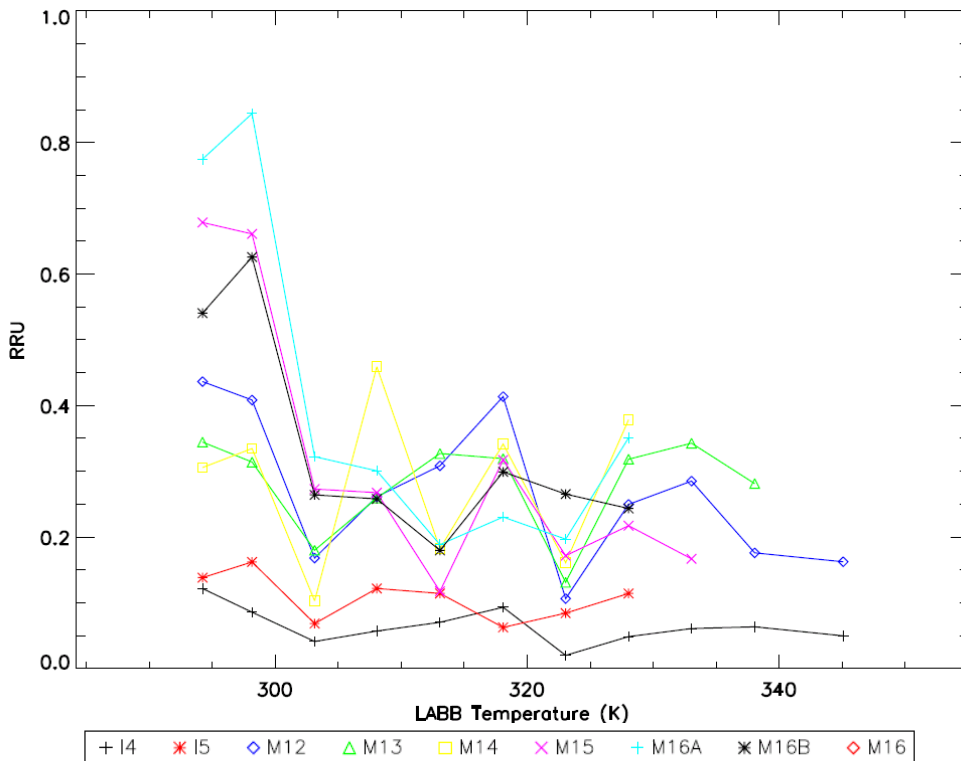


Figure 29: worst case detector RRU versus scene temperature [K] for electronics side A and a cold focal plane temperature of 82.5 K.



+ 1 \* 2 ◊ 3 △ 4 □ 5 × 6 + 7 ✖ 8 ◊ 9 △ 10 □ 11 × 12 + 13 ✖ 14 ◊ 15 △ 16

□ 17 × 18 + 19 ✖ 20 ◊ 21 △ 22 □ 23 × 24 + 25 ✖ 26 ◊ 27 △ 28 □ 29 × 30 + 31 ✖ 32

+ 1 \* 2 ◊ 3 △ 4 □ 5 × 6 + 7 ✖ 8 ◊ 9 △ 10 □ 11 × 12 + 13 ✖ 14 ◊ 15 △ 16